Multidimensional intermolecular dynamics from tunable far-infrared laser spectroscopy: Angular-radial coupling in the intermolecular potential of argon–H_2O

R. C. Cohen[a] and R. J. Saykally
Department of Chemistry, University of California, Berkeley, California 94720

(Received 17 June 1991; accepted 20 August 1991)

Five new vibration–rotation tunneling states of Ar–H_2O [the Σ and $\Pi(1_{11})$ and the Σ and $\Pi(2_{12})$ internal rotor states and the $n = 1$, $\Pi(1_{01})$ stretching-internal rotor combination level] have been accessed by tunable far-infrared laser spectroscopy. The measured vibrational band origins of transitions to these states are within 2% of predictions made from an anisotropic three-dimensional intermolecular potential surface (denoted AW1) derived from a nonlinear least-squares fit to previous far-infrared spectral data [J. Phys. Chem. **94**, 7991(1990)]. This provides strong evidence that the AW1 intermolecular potential surface incorporates much of the essential physics of the intermolecular forces which bind the cluster. However, larger deviations from the predictions are found in the observed rotational term values. A detailed analysis of these deviations clearly demonstrates the need for even stronger angular-radial coupling in the Ar–H_2O intermolecular potential than the already substantial coupling present in the AW1 surface. Specifically, the presently observed $\Sigma(1_{11})$ state and the $n = 1$, $\Sigma(0_{00})$ state are found to be approximately 65:35 mixtures of the basis states which represent pure stretching and internal rotation. The $\Sigma(2_{12})$ level is found to be mixed just as strongly with $n = 2$, $\Sigma(1_{01})$. The formalism for accurately deperturbing vibration–rotation–tunneling states coupled by Coriolis interactions used in the above analysis is presented.

INTRODUCTION

The Ar–H_2O complex is among the simplest of all molecular clusters. It has become an important prototype in the quest for understanding the multidimensional intermolecular potential-energy surfaces (IPS's) and associated dynamics that govern the behavior of chemically important, but much more complicated, clusters like the water dimer and the ammonia dimer. It also serves as a convenient vehicle for testing existing theories of intermolecular forces, and its IPS is relevant for the simulation of hydrophobic interactions in model systems. In two recent papers,[1,2] we have described the application of tunable far-infrared (TFIR) laser spectroscopy to the measurement of the intermolecular vibration–rotation–tunneling (VRT) spectrum of Ar–H_2O. Using these data, we have developed an accurate description of the three-dimensional anisotropic intermolecular potential characterizing the interaction of argon with a water molecule in its ground vibrational state.[3] This potential, denoted AW1, is shown in Figs. 1–3. The experiments described in this paper have been performed to provide a thorough test of the accuracy of this three-dimensional IPS. Two conclusions may be drawn from an approximate analysis of the experimental results described herein: (1) the AW1 surface accurately represents the intermolecular forces acting between argon and water; (2) although the angular-radial coupling in the AW1 surface is strong, leading to substantial mixing of internal rotor and stretching states of the complex, even stronger angular-radial coupling is required in the IPS to precisely account for the newly observed bands measured in this work. Angular-radial coupling may be loosely described as variations in the position (distance of the argon from the center of mass of water) of the radial minimum as a function of the relative orientation of the two subunits. It results from anisotropy in both the attractive and the repulsive forces, but is expected to be dominated by the latter, which vary exponentially. On the AW1 surface, the potential minimum for the argon approaching in the plane of the water along the C_{2v} axis from the hydrogen end occurs at a distance of about 3.75 Å. This distance decreases more or less smoothly as the H_2O subunit is rotated. In the planar C_{2v} Ar–OH_2 configuration, the potential minimum is at 3.55 Å. The measurements described in this paper require stronger angular-radial coupling, implying either that the magnitude of the variation in the position of the radial minimum is larger than that indicated by this 0.2 Å difference, or that there is not quite so smooth a variation as the monomer rotates.

In our first study of Ar–H_2O,[1] we reported the measurement of two bending vibrations (at 21.26 and 24.62 cm^{-1}) which contained information about the anisotropy of the IPS in the region of the potential minimum. These bands were subsequently interpreted in accord with a model for the internal dynamics in the two angular coordinates (θ,ϕ) proposed by Hutson.[4] We then measured two intermolecular stretching vibrations,[2] the fundamental [$n = 1$, $\Sigma(0_{00}) \leftarrow n = 0$, $\Sigma(0_{00})$] at 30.45 cm^{-1}, and a stretching band built on the lowest excited internal rotor state [$n = 1$, $\Sigma(1_{01}) \leftarrow n = 0, \Sigma(1_{01})$] at 33.88 cm^{-1}. These spectra place experimental constraints on the shape of the IPS in the radial coordinate (R). The internal coordinates used to describe the intermolecular dynamics of Ar–H_2O are a set of body-fixed Jacobi coordinates specifying the orientation of the ar-

[a] Present address: Department of Chemistry, Harvard University, Cambridge, Massachusetts 02138.

 0021-9606/91/237891-16$03.00

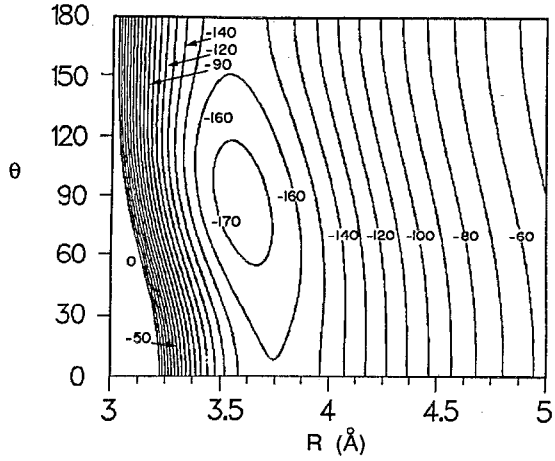

FIG. 1. The AW1 intermolecular potential-energy surface for Ar–H_2O. R is the vector from the center of mass of the water monomer to the argon and θ is the angle between this vector and the water monomer C_{2v} axis. For this plot $\phi = 0$, constraining the complex to be planar. Contours are drawn at 10 cm^{-1} intervals referenced to a zero of energy at the dissociation energy. Contours above this energy are omitted for clarity.

gon with respect to a water molecule fixed at its vibrationally averaged ground-state geometry. The three large-amplitude coordinates are the vector from the center of mass of the water to the argon (R), the angle between the C_{2v} axis of the water molecule (θ) and the vector R, and the angle describing the rotation of the water about its C_{2v} axis (ϕ). At $\theta = 0°$ the argon is situated along the C_{2v} axis and nearest to the hydrogens. At $\theta = 180°$, the argon is closest to the oxygen end of the molecule. The reference geometry for $\phi = 0°$ is chosen to be one in which all four atoms are coplanar. At $\theta = 0°$ or 180°, the interaction is independent of ϕ, since rotation about the C_{2v} axis of the water with θ fixed at these angles does not affect the relative orientation of the two subunits.

Initial attempts to understand the VRT spectra relied on approximate dynamical models which treated the angular and radial degrees of freedom as separable. Hutson[4] developed a series of effective angular potentials describing the barriers to internal motion of the H_2O subunit within the complex, averaged over the radial motion of the ground in-

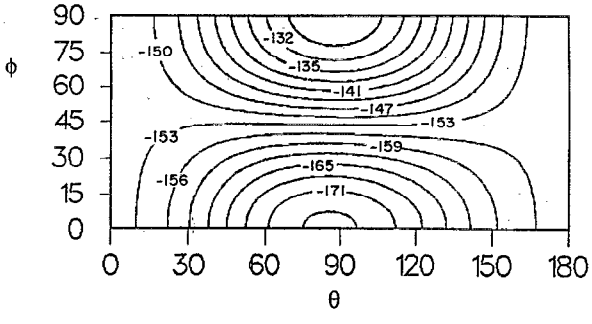

FIG. 2. The AW1 IPS at $R = 3.6$ Å.

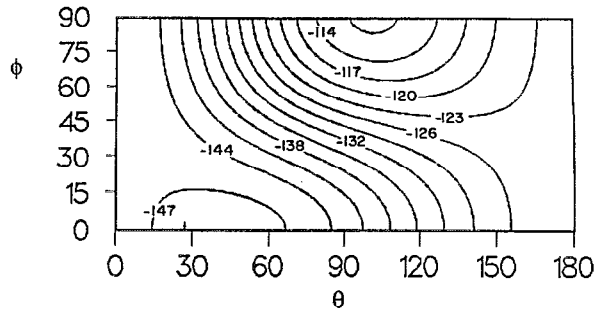

FIG. 3. The AW1 IPS at $R = 4.0$ Å.

termolecular stretching state. Based on the Coriolis analysis which we presented in Ref. 2, Hutson was able to suggest that one of the several different potentials was more likely to represent the true surface than were the others. This potential has a minimum with the argon located in the plane of the water, oriented such that the van der Waals bond axis is oriented at 90° to the C_{2v} axis of water. It has a barrier of about 40 cm^{-1} at $\theta = 90°$, $\phi = 90°$, the orientation at which the argon atom sits directly above the H_2O plane, and has barriers to rotation in the plane of the water of 15 cm^{-1} at both the Ar–H_2O and the Ar–OH_2 geometries. In our own work, presented in Ref. 2, we developed a series of effective radial potentials for three of the measured Σ internal rotor states, estimating the anisotropic well depth to be approximately 150 cm^{-1} by assuming that the deepest effective radial potential samples the absolute minimum on the three-dimensional anisotropic IPS. The validity of both the angular model of Hutson[4] and our own effective radial potentials[2] is predicated on the approximate separability of the angular and the radial coordinates. The observation that the two stretching frequencies measured in Ref. 2 were located 3.4 cm^{-1} apart was the first experimental indication that these coordinates are not even approximately separable in this complex. This 3.4 cm^{-1} difference is more than 10% of the stretching frequency. Although, we mentioned this fact in Ref. 2, its importance was not fully appreciated at that time. It indicates a large perturbation to one or both states and underscores the need for rigorous treatment of the dynamics in even the simplest weakly bound complexes.

Direct fits of the experimental data to obtain a three-dimensional IPS were not performed when these data were collected because of both the significant computational expense and the complexity of the programming required to accurately calculate the eigenvalues of the multidimensional Hamiltonian for the internal and the overall rotational motions. Subsequently (Ref. 3), we developed an adaptation of the collocation method, which was successfully employed for molecular eigenstate calculations by Peet and Yang,[5–8] to rotating three-dimensional systems. The collocation method is a simple and efficient method for accurately computing the eigenvalues and the eigenvectors corresponding to VRT states of weakly bound complexes. It was used previously to obtain the energies and the wave functions of Ar–CO_2,[8] Ar–HCl,[6,7] and Ar–H_2O.[3] The computational simplicity is

especially appealing. For example, excluding the potential subroutine and the matrix eigenvalue routine, Peet and Yang[6] obtain the Ar–HCl eigenvalues to an accuracy of 0.001 cm^{-1} with less than 150 lines of code. The Ar–H_2O eigenvalue subroutine, which was developed in Ref. 3, has been embedded in a nonlinear least-squares loop and used to perform a direct fit to the experimental VRT energy differences involving the total angular momentum states $J=0$ and $J=1$. The resulting three-dimensional IPS for Ar–H_2O (denoted AW1) has a 174.7 cm^{-1} minimum corresponding to a planar structure with the water symmetry axis oriented nearly perpendicular to the vector joining the centers of mass ($R=3.598$ Å). In the region of the minimum, the AW1 potential is very flat. Barriers to motion of the argon in the plane of the H_2O are about 22 cm^{-1} at the Ar–OH_2 configuration and 17 cm^{-1} at the Ar–H_2O configuration. The largest barrier occurs for motion out of the plane. There is a 47 cm^{-1} barrier for having the argon located directly above the plane of the water. These aspects of the surface are similar to those obtained by Hutson, suggesting that the interaction is at least qualitatively described by an approximate two-dimensional analysis. Two other significant features are evident in the AW1 IPS, which are not accessible in the two-dimensional angular surface; both of these contribute to the strong angular-radial coupling that mixes pure internal rotor and pure stretching basis states, which otherwise constitute an excellent zeroth-order approximation to wave functions describing the intermolecular dynamics. First, there is significant variation in the position of the repulsive wall with the angle of approach of the argon. At the dissociation energy, the argon can approach nearly 0.2 Å closer to the H_2O center of mass at the oxygen end of the molecule than at the hydrogen end (see Fig. 1). Second, the long-range attractive forces are a maximum at orientations in which the argon is closest to a hydrogen atom. This is indicated in Figs. 2 and 3, which show the angular portion of the surface at $R=3.6$ Å and at $R=4.0$ Å. The effects of the exponential repulsion are substantially reduced at 4.0 Å, so this plot primarily reflects the attractive anisotropy. These attractive forces are shown to favor a linear hydrogen-bonded orientation for the complex. Analysis of the contributions of the different anisotropic components (induction, dispersion, and repulsion) to the shape of the IPS could not be inferred from a one- or two-dimensional approximate treatment of the intermolecular dynamics.

The limited experimental data set used in developing the AW1 surface permitted accurate determination of nine different parameters in a series expansion of the IPS; the higher-order terms were all arbitrarily fixed to zero. To the extent that the series expansion of the potential is rapidly converging, these parameters represent an adequate description of the intermolecular forces present in the interaction of argon with water. However, with the exception of the AW1 surface, accurate anisotropic IPS's have been derived only for a few atom-linear molecule complexes,[9] and a universal understanding of the rate of convergence or optimum form of model IPS's has not yet emerged from such work. An accurate and detailed characterization of intermolecular forces in Ar–H_2O requires experimental confirmation of the convergence of the potential expansion. Toward this end, we have measured five new bands of Ar–H_2O. These measurements, in themselves, double the size of the data set used to develop the AW1 surface, and provide an exacting test of its accuracy.

Ar–H_2O has also been the subject of several other experimental studies since the development of the AW1 IPS. The microwave studies of Fraser *et al.*[10] established more precise rotational term values for the normal isotope and determined rotational term values for several other isotopic species. That group also measured μ_a, the dipole moment of the ground state [$\Sigma(0_{00})$], set an upper limit to the value of μ_a in the first excited internal rotor level [$\Sigma(1_{01})$], and measured the nuclear quadrupole coupling constants of Ar–H_2 ^{17}O. In other microwave work, Gutowsky and coworkers[11] experimentally confirmed the assignment of the $\Sigma(1_{01})$ state as arising from *ortho*-Ar–H_2O through measurement of the triplet hyperfine structure associated with the spin–spin interaction of the two hydrogen nuclei. Lascola and Nesbitt[12] measured the fundamental asymmetric stretch of the H_2O subunit in the near-infrared spectrum of Ar–H_2O. These measurements provide data from which an understanding of the dependence of the IPS on the *intra*molecular degrees of freedom can begin to be developed, and they characterize the nature of energy transfer between the two energetically similar OH stretching levels. Lascola and Nesbitt also determined the relative energy of the $J=1$, $B_1\Sigma(1_{01})$ and $J=1$, $B_2\Pi(1_{01})$ states on the ground-state surface to be 339.763(9) GHz from infrared combination differences. This observation compares quite favorably with our prediction of 344 GHz, made from the AW1 potential surface.[3] In addition to these measurements, Suzuki *et al.*[13] and Zwart and Meerts[14] have reported measurement of far-infrared VRT transitions in Ar–D_2O and Ar–HDO.

There has also been considerable recent theoretical interest in the Ar–H_2O complex. Pressure-broadening cross sections calculated on the AW1 surface by Green[15] are about 15% lower than the experimental cross sections[16] (just outside the error bars on the experimental data). Green has suggested that anisotropy in β, the exponent which determines the slope of the repulsive wall, may be required in the IPS to more adequately describe the experimental pressure-broadening cross sections. The anisotropy in β was fixed to zero in the AW1 surface. *Ab initio* calculations of the Ar–H_2O interaction have been performed by Chalisinski, Szczesniak, and Scheiner[17] and by Bulski *et al.*[18] The calculations by Chalisinski, Szczesniak, and Scheiner produce anisotropy in the IPS which is similar to that present in the experimental AW1 surface. Both have a broad, flat minimum with the H_2O C_{2v} axis nearly perpendicular to the van der Waals bond and all four atoms coplanar. The equilibrium structure on both *ab initio* surfaces places the argon in the plane of the water molecule, oriented so that the threefold hollow formed by one OH bond and the two nonbonding lone pairs is closest to the argon atom. As in the AW1 surface, the dominant attractive and repulsive anisotropic forces occur in the vicinity of the hydrogens. The anisotropic repulsion in the *ab initio* surfaces is clearly smaller between the two hydrogen atoms, allowing closer approach of the

TABLE I. Observed transitions (MHz) and residuals from the least-squares fits in the $n = 1$, $\Pi(1_{01}) \leftarrow \Sigma(1_{01})$ band.

$J' \leftarrow J''$	Observed frequency	Residuals
3←4	1 313 388.0	0.3
2←3	1 319 982.0	−0.7
1←0	1 343 788.2	0.2
1←1	1 337 782.9	−0.2
2←2	1 336 908.9	0.6
3←3	1 335 590.9	0.0
4←4	1 333 824.3	−0.1
5←5	1 331 600.3	−0.1
6←6	1 328 908.3	−0.1
7←7	1 325 736.1	0.2
9←9	1 317 889.7	−0.1
10←10	1 313 181.5	0.1
11←11	1 307 923.2	0.0
14←14	1 288 621.3	0.0

TABLE II. Observed transitions (MHz) and residuals from the least-squares fits in the $\Pi(1_{11}) \leftarrow \Sigma(0_{00})$ and $\Sigma(1_{11}) \leftarrow \Sigma(0_{00})$ bands.

$J' \leftarrow J''$	Observed frequency $\Pi(1_{11}) \leftarrow \Sigma(0_{00})$	Residuals	Observed frequency $\Sigma(1_{11}) \leftarrow \Sigma(0_{00})$	Residuals
11←12	1 014 438.4	−0.1		
10←11	1 023 971.6	0.1	1 156 580.6	0.0
9←10	1 033 065.6	1.6	1 161 793.7	1.6
8←9			1 167 184.5	0.4
7←8	1 050 023.4	3.7	1 172 731.7	−0.4
6←7	1 057 937.6	4.2	1 178 410.3	−0.8
5←6	1 065 509.2	2.6	1 184 194.7	−0.7
4←5	1 072 769.5	3.5	1 190 059.1	−0.7
3←4	1 079 738.6	2.5	1 195 982.1	1.3
2←3	1 086 437.4	−1.1	1 201 937.7	0.7
1←2	1 092 886.4	−3.6	1 207 911.5	0.4
0←1	⋯		1 213 890.1	−0.1
1←0	1 110 813.6	−2.6	1 225 836.5	−0.9
2←1	1 116 305.0	−2.9	1 231 806.0	−0.4
3←2	1 121 534.5	−2.6		
4←3	1 126 479.0	−3.3		
5←4	1 131 115.2	−2.3		
6←5	1 135 411.6	−1.9	1 255 892.4	1.2
7←6	1 139 336.6	−2.3	1 262 051.7	0.4
8←7	1 142 858.2	−4.0	1 268 307.5	−0.2
9←8			1 274 679.0	−1.8
1←1	1 105 094.0	1.3		
2←2	1 105 122.0	1.7		
3←3	1 105 161.6	−0.4		
4←4	1 105 217.8	0.1		
5←5	1 105 288.4	0.5		
6←6	1 105 371.0	−1.6		
7←7	1 105 472.0	−0.3		
8←8	1 105 587.2	−1.4		
9←9	1 105 717.0	−0.9		
10←10	1 105 864.8	0.1		
11←11	1 106 028.7	0.4		
12←12	1 106 209.9	0.7		
13←13	1 106 408.8	0.9		
14←14	1 106 625.9	0.6		
15←15	1 106 862.5	0.5		
16←16	1 107 117.7	−1.2		

argon along this orientation than in the hydrogen-bonded orientation. However, in the experimental AW1 surface the repulsive forces do not decrease between the hydrogens, since the form of the potential was not sufficiently flexible and the experimental data did not explicitly require such anisotropy. Other features of the two surfaces are also different, especially the absolute well depth, which is 175 cm^{-1} on the AW1 surface. Chalisinski, Szczesniak, and Scheiner estimate that the true well depth is 25% deeper than the 108 cm^{-1} indicated by their calculations. While this is significantly shallower than the AW1 well depth, the two are not necessarily inconsistent since the experimental well depth is highly correlated with the parameter describing the slope of the repulsive wall (β).

In the present paper, we describe new experimental measurements which provide a critical test of the AW1 surface. Five new VRT bands have been measured: the $\Sigma(1_{11}) \leftarrow \Sigma(0_{00})$, $\Pi(1_{11}) \leftarrow \Sigma(0_{00})$, $\Sigma(2_{12}) \leftarrow \Sigma(1_{01})$, $\Pi(2_{12}) \leftarrow \Sigma(1_{01})$, and the $n = 1$, $\Pi(1_{01}) \leftarrow \Sigma(1_{01})$ bands (Tables I–III). The labeling of the states is represented by n (the number of quanta of stretching excitation), which for simplicity we omit when $n = 0$, $\Omega = \Sigma,\Pi,\Delta,...$ (the projection of the total angular momentum J, and identically, the projection of internal angular momentum j, on the pseudo-diatomic axis), and j_{kakc} (the free rotor level of the H_2O subunit to which the internal rotor state most nearly correlates). The individual components of the doubly Π degenerate states may also be identified by their full VRT symmetry in the molecular symmetry group of the complex, if necessary. For Ar–H_2O, this group is isomorphic to the C_{2v} point group, which has four irreducible representations: A_1, A_2, B_1, B_2. Figure 4 presents an overview of the experimentally determined VRT energy differences in Ar–H_2O, along with the calculated positions of all other levels of Ar–H_2O which are bound by more than 30 cm^{-1}. Most importantly, the new data clearly demonstrate that the already strong angular-radial coupling present in the AW1 surface is nevertheless not strong enough. Since this angular-radial coupling results primarily from the anisotropy in the position of the repulsive wall in the AW1 surface, we conclude that there must be additional anisotropic structure in this region of the surface beyond that indicated in the AW1 model.

EXPERIMENT

The tunable far-infrared laser used in these experiments has been described in detail by Blake *et al.*[19,20] Tunable far-infrared radiation is generated by mixing the output from a narrow-band (<100 kHz) fixed-frequency optically pumped far-infrared laser with the output of a microwave synthesizer (HP8673B) or its harmonics in a Schottky barrier diode (University of Virginia, No. 1I7). Microwaves in the range 2–60 GHz are coaxially coupled onto the diode, while frequencies in the range 60–110 GHz are coupled with waveguide. The resulting 10–100 μW generated at the sum and difference frequencies ($\omega_{laser} \pm n\omega_{microwaves}$, $n = 1,2,3,...$) are separated from the much stronger fixed-frequency laser (10–500 mW) using a polarizing Michelson interferometer. The tunable sideband radiation is then focused into a multipass cell of the type developed by Perry and co-workers,[21] where it makes about ten passes through

TABLE III. Observed transitions (MHz) and residuals from the least-squares fits in the $\Pi(2_{12})\leftarrow\Sigma(1_{01})$ and $\Sigma(2_{12})\leftarrow\Sigma(1_{01})$ bands.

$J\leftarrow J$	Observed frequency	Residuals
$\Pi(2_{12})\leftarrow\Sigma(1_{01})$		
10←11	1 773 219.3	−0.1
9←10	1 781 529.5	0.1
7←8	1 794 711.0	−0.1
4←5	1 809 359.5	1.0
3←4	1 813 803.1	−0.3
2←3	1 818 385.4	1.6
1←2	1 823 269.8	−2.5
1←0	1 840 745.0	1.4
2←1	1 847 498.0	0.3
3←2	1 854 552.5	−0.2
4←3	1 861 730.8	−1.8
5←4	1 868 830.0	0.0
6←5	1 875 620.1	0.8
7←6	1 881 864.3	−0.5
10←9	1 894 963.0	0.0
1←1	1 834 247.7	0.6
2←2	1 833 909.4	−2.1
3←3	1 833 412.5	2.2
4←4	1 832 745.3	−0.2
5←5	1 831 920.0	−0.5
6←6	1 830 937.8	−0.9
7←7	1 829 805.0	1.3
8←8	1 828 517.8	−0.9
9←9	1 827 085.1	−0.1
10←10	1 825 503.4	1.1
11←11	1 823 764.1	0.1
12←12	1 821 855.9	−1.1
13←13	1 819 757.1	0.0
14←14	1 817 425.4	0.6
15←15	1 814 799.1	−0.2
$\Sigma(2_{12})\leftarrow\Sigma(1_{01})$		
9←10	1 592 388.0	−0.1
8←9	1 604 963.9	0.0
8←7	1 703 668.0	−0.1
9←8	1 702 614.0	0.0

the long axis of a planar supersonic jet. Several different laser lines were employed in these experiments: 1016.8972 GHz (CH_3OD), 1042.1504 GHz (CH_2F_2), 1101.1594 GHz (CH_2DOH), 1193.7273 GHz (CH_3OH), 1299.9969 GHz (CH_3OD), 1626.6026 GHz (CH_2F_2), 1757.5263 GHz (CH_3OH), 1838.8393 GHz (CH_3OH), and 1891.2743 (CH_3OH).

As in our previous studies of Ar–H_2O,[1,2] the cluster is generated by passing argon over water in a reservoir and then expanding the mixture through the planar nozzle. The current version is a 4.0 in.×0.001 in. nozzle described in detail by Busarow.[22] It gives more than a factor of 2 increase in signal over the earlier 1.5 in. long design. After passing through the Perry cell, the far-infrared laser radiation is focused onto a Putley mode InSb detector for the experiments near 1100–1400 GHz, or a stressed Ga:Ge photoconductor for the experiments above 1500 GHz. Signals are detected by frequency modulation of the laser and demodulation of the detector output at $2f$.

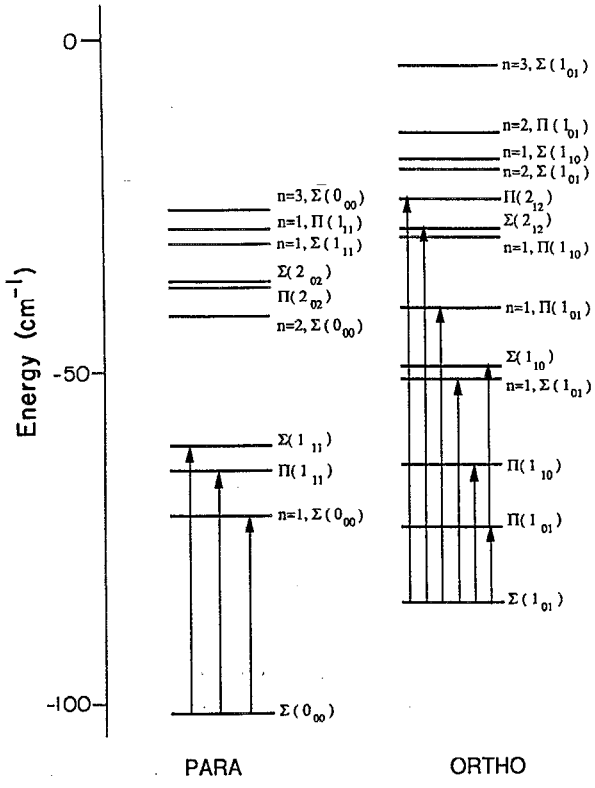

FIG. 4. The energy-level diagram of the $J=1$ VRT states of Ar–H_2O as calculated on a modified version of the AW1 IPS.

RESULTS

In Fig. 5, we present a computer-generated stick spectrum of the nine different bands of Ar–H_2O which have been observed by far-infrared VRT spectroscopy. The spectrum is nearly continuous, with VRT absorptions extending more or less uniformly from 550 to 1900 GHz (16–63 cm^{-1}). In Figs. 6 and 7, we show examples of transitions in the $n=1$, $\Pi(1_{01})\leftarrow\Sigma(1_{01})$ and $\Pi(2_{12})\leftarrow\Sigma(1_{01})$ bands. The intensities in the stick spectrum are calculated for a 5 K beam and

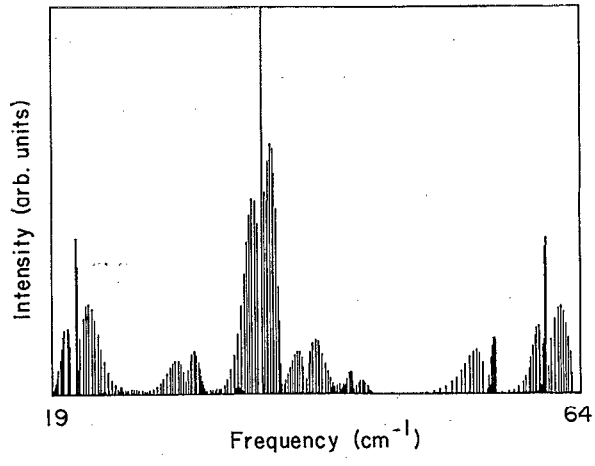

FIG. 5. Computer-generated VRT spectrum of the observed bands of Ar–H_2O at 5 K.

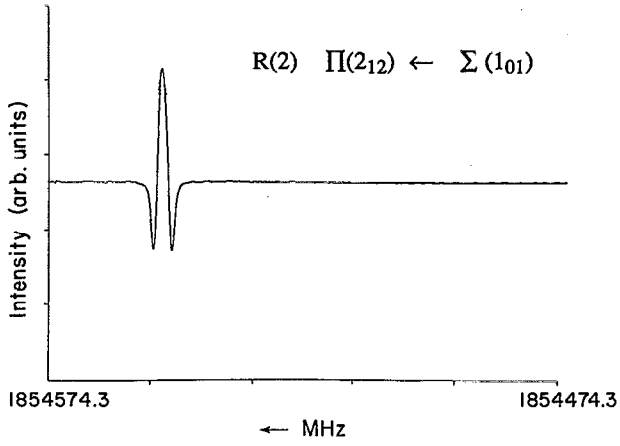

FIG. 6. The $R(2)$ line in the $\Pi(2_{12}) \leftarrow \Sigma(1_{01})$ band. This scan and the one in Fig. 7 are obtained with a 300 ms RC time constant scanning at a rate of 0.3 MHz/s.

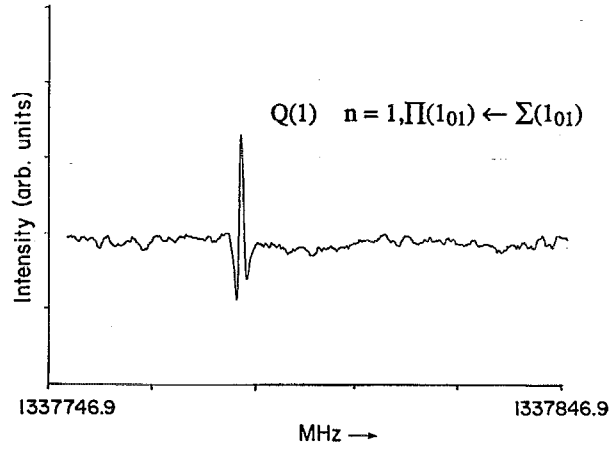

FIG. 7. The $Q(1)$ line in the $n = 1$, $\Pi(1_{01}) \leftarrow \Sigma(1_{01})$ band.

take into account the transition frequency and degeneracy factors which contribute to the experimental intensities. Several other transitions with sufficient intensity to be observed are predicted to occur in this region, but only the bands that have actually been observed are plotted. The overall intensity of each band has been scaled by the square of the transition moment for the $R(0)$ line [except for the $\Sigma \leftarrow \Pi$ band for which we scale using the $P(1)$ line] as calculated on a modified AW1 surface. No correction for intensity perturbations leading to abnormal relative intensities in the P, Q, and R branches has been applied, although such effects are expected because of the presence of significant vibrational angular momentum and strong Coriolis coupling.

Searches for the new bands (Tables I–III) reported in this work were guided by our predictions from the AW1 surface. The observed $R(0)$ transitions of the two 1_{11} bands were found at 1110.816 and 1225.837 GHz—within 2 and 14 GHz, respectively, of the frequencies predicted using the AW1 surface, viz. 1112 and 1212 GHz. The $\Pi(2_{12})$ $R(0)$ transition was observed at 1840.745 GHz and the $\Sigma(2_{12})$ $R(0)$ transition, which has not been observed, is estimated to be at 1690($\pm$ 10) GHz, from the fit to high J lines in the $\Sigma(2_{12})$ band. Again, the Π state was predicted more accurately than the Σ state on the AW1 surface; these predictions respectively occurring at 1853 and 1740 GHz. The $n = 1$, $\Pi(1_{01}) \leftarrow \Sigma(1_{01})$ $R(0)$ transition was observed at 1343.788 GHz compared to the prediction of 1324 GHz.

In Table IV we present a detailed comparison of VRT transitions and rotational term values computed on the AW1 IPS with the current experimental data set for Ar–H_2O. The newly measured vibrational frequencies and rotational term values were predicted to within 3%. However, much larger deviations from the predictions are evidenced in the l-type splittings in the Π states. These measurements precisely specify the wave functions of the states involved and will ultimately contribute to a more accurate description of the angular-radial coupling in an improved experimental IPS. The differences between the experimental and the AW1 $J = 2 \leftarrow 1$ term values clearly indicate two different types of deficiencies in the IPS. Both the $\Pi(1_{11})$ and $\Pi(2_{12})$ states have one parity component predicted accurately, while the other is predicted very poorly. As discussed in detail below, the only term in the Hamiltonian which splits the otherwise degenerate components of the Π and Δ ($\Omega = 1$ and $\Omega = 2$) states is the Coriolis interaction. The Coriolis matrix element is diagonal in all quantum numbers, with the exception of Ω. Its strongest effect is to mix (and thereby shift) Σ and Π states of the same J and rovibrational symmetry. The component of $\Pi(1_{11})$ and $\Pi(2_{12})$ which is poorly predicted is the one of the same rovibrational symmetry as the associated Σ state. In both cases, the shifted component is predicted using the AW1 surface to be farther away from its partner of the opposite parity than was actually measured, i.e., the Coriolis interaction is too large on the AW1 surface. Moreover, the Coriolis effect on AW1 is already reduced substantially from that expected if the angular and radial degrees of freedom were approximately separable, as in Hutson's treatment. The reason for the deviation of experimental term values from the AW1 predictions is that the already strong angular-radial coupling present in it is actually too weak! Angular-radial coupling in the IPS affects the wave functions of the $\Sigma(1_{11})$ and the $\Sigma(2_{12})$ states by strongly mixing them with near-resonant stretching levels of the same symmetry [$n = 1$, $\Sigma(0_{00})$ and $n = 2$, $\Sigma(1_{01})$; see Fig. 4 and Table IV for the specific symmetries]. The Coriolis interaction between these states and the associated Π states is thus reduced. The size of the Coriolis-induced splittings we have measured indicates that this effect is underestimated by the AW1 potential. The second obvious shortcoming of the AW1 surface is indicated by the $J = 2 \leftarrow 1$ rotational term values of the $\Pi(1_{10})$ and $n = 1$, $\Pi(1_{01})$ states. In these states, the difference between the observed and the AW1 rotational term values is about the same for all parity components. The rotational term values in $\Pi(1_{10})$ are computed to be too large indicating the effective bond length in this state is too short. For the $n = 1$, $\Pi(1_{01})$, the computed term values are too small indicating the AW1 bond length is too long. This indicates that the effective radial surface sampled by these states is not adequately represented by the AW1 model: $\Pi(1_{10})$ samples pri-

TABLE IV. Comparison of the predicted energy differences on the AW1 IPS (Ref. 3) and the measured energy differences for Ar–H_2O.

		Calculated on AW1 IPS	Experimental	Residuals
Rotational term values (MHz)				
$J=1\leftarrow0$				
$\Sigma(0_{00})$	$A_2\leftarrow A_1$	5 970.4	5 975.8[a]	5.4
$n=1,\Sigma(0_{00})$	$A_2\leftarrow A_1$	5 678.6	5 676.5[a]	−2.1
$\Sigma(1_{11})$	$A_2\leftarrow A_1$	6 186.2	5 971.1	−215.1
$\Sigma(1_{01})$	$B_1\leftarrow B_2$	5 828.2	5 824.2[a]	−4.0
$n=1,\Sigma(1_{01})$	$B_1\leftarrow B_2$	5 460.0	5 461.6[a]	1.6
$\Sigma(1_{10})$	$B_2\leftarrow B_1$	6 053.9	6 052.8[a]	−1.1
$\Sigma(2_{12})$	$B_1\leftarrow B_2$	4 262.5	...	...
$J=1\leftarrow1$				
$\Pi(1_{11})$	$A_1\leftarrow A_2$	362.1	252.6	−110.5
$\Pi(1_{01})$	$B_1\leftarrow B_2$	205.1	205.0[a]	−0.1
$n=1,\Pi(1_{01})$	$B_1\leftarrow B_2$	196.0	181.0	−15.0
$\Pi(1_{10})$	$B_1\leftarrow B_2$	146.7	146.8[a]	0.1
$\Pi(2_{12})$	$B_1\leftarrow B_2$	1 559.3	672.3	−887.0
$J=2\leftarrow1$				
$\Sigma(0_{00})$	$A_1\leftarrow A_2$	11 938.3	11 950.1	11.8
$n=1,\Sigma(0_{00})$	$A_1\leftarrow A_2$	11 355.9	11 351.4	−4.5
$\Sigma(1_{11})$	$A_1\leftarrow A_2$	12 369.3	11 945.3	−424.0
$\Pi(1_{11})$	$A_1\leftarrow A_2$	11 254.0	11 467.8	213.8
$\Pi(1_{11})$	$A_2\leftarrow A_1$	11 978.7	11 977.7	−1.0
$\Sigma(1_{01})$	$B_2\leftarrow B_1$	11 654.7	11 647.0	−7.7
$\Pi(1_{01})$	$B_2\leftarrow B_1$	12 215.7	12 214.2	−1.5
$\Pi(1_{01})$	$B_1\leftarrow B_2$	11 806.1	11 804.8	−1.3
$n=1,\Sigma(1_{01})$	$B_2\leftarrow B_1$	10 918.4	10 920.6	2.2
$n=1,\Pi(1_{01})$	$B_2\leftarrow B_1$	11 492.2	11 132.5	−359.7
$n=1,\Pi(1_{01})$	$B_1\leftarrow B_2$	11 101.1	10 772.3	−328.8
$\Pi(1_{10})$	$B_2\leftarrow B_1$	12 048.3	12 148.9	100.6
$\Pi(1_{10})$	$B_1\leftarrow B_2$	11 755.3	11 855.4	100.1
$\Sigma(1_{10})$	$B_1\leftarrow B_2$	12 105.1	12 103.0	−2.1
$\Sigma(2_{12})$	$B_2\leftarrow B_1$	8 643.4	...	...
$\Pi(2_{12})$	$B_2\leftarrow B_1$	14 229.9	12 577.3	−1 652.6
$\Pi(2_{12})$	$B_1\leftarrow B_2$	11 247.6	11 308.8	61.2
$J=2\leftarrow2$				
$\Pi(1_{11})$	$A_2\leftarrow A_1$	1 086.8	762.5	−324.3
$\Pi(1_{01})$	$B_2\leftarrow B_1$	614.7	614.4	−0.1
$n=1,\Pi(1_{01})$	$B_2\leftarrow B_1$	587.1	541.2	−45.9
$\Pi(1_{10})$	$B_2\leftarrow B_1$	439.7	440.3	0.9
$\Pi(2_{12})$	$B_2\leftarrow B_1$	4 541.6	1 939.7	−2 602.5
Vibrational transitions (GHz)				
$n=1,\ \Sigma(0_{00})\leftarrow\Sigma(0_{00})$	$A_2\leftarrow A_1\ J=1\leftarrow0$	913.3	913.0[a]	−0.3
$\Pi(1_{11})\leftarrow\Sigma(0_{00})$	$A_2\leftarrow A_1\ J=1\leftarrow0$	1 112.4	1 110.8	−1.6
$\Sigma(1_{11})\leftarrow\Sigma(0_{00})$	$A_2\leftarrow A_1\ J=1\leftarrow0$	1 212.3	1 225.8	13.5
$\Pi(1_{01})\leftarrow\Sigma(1_{01})$	$B_1\leftarrow B_2\ J=1\leftarrow0$	349.6	345.8[b]	−3.8
$n=1,\ \Sigma(1_{01})\leftarrow\Sigma(1_{01})$	$B_1\leftarrow B_2\ J=1\leftarrow0$	1 024.5	1 024.7[a]	0.2
$\Pi(1_{10})\leftarrow\Sigma(1_{01})$	$B_1\leftarrow B_2\ J=1\leftarrow0$	637.3	637.4[a]	0.2
$n=1,\ \Pi(1_{10})\leftarrow\Sigma(1_{01})$	$B_1\leftarrow B_2\ J=1\leftarrow0$	1 323.7	1 343.8	20.1
$\Sigma(2_{12})\leftarrow\Sigma(1_{01})$	$B_1\leftarrow B_2\ J=1\leftarrow0$	1 739.6	1 690.(10)[c]	−49.0
$\Pi(2_{12})\leftarrow\Sigma(1_{01})$	$B_1\leftarrow B_2\ J=1\leftarrow0$	1 853.3	1 840.7	−12.6
$\Sigma(1_{10})\leftarrow\Pi(1_{01})$	$B_1\leftarrow B_2\ J=0\leftarrow1$	737.9	738.0[a]	0.2

[a] Included in the fit to derive the AW1 surface.
[b] Reference 12.
[c] Estimated uncertainty in parentheses.

marily the region of the potential minimum, and the $n=1$, $\Pi(1_{01})$ state samples primarily the geometry at which the argon lies directly above the plane of the H_2O. Apparently the AW1 surface can be improved at several different orientations. All of the other differences between the observed spectra and the predictions on the AW1 surface may be ascribed to one or both of these types of inadequacies in the IPS. The relatively accurate predictions for the Π-state components which do not interact with the companion Σ states, and the errors in the VRT frequencies shown in Table IV, could be interpreted to imply that the Π states are more accurately modeled on the AW1 surface than are the Σ states. However, it is more likely that the Π states are less sensitive to the details of the surface, since there are not as many near resonances between Π internal rotor and Π stretching states as there are between Σ internal rotor and stretching states. Because no Π states can be derived from $j=0$ internal rotor levels, this same conclusion is likely to apply to a wide variety of van der Waals complexes.

CORIOLIS EFFECTS

Even an approximate understanding of the physical basis for the observed Ar–H_2O spectra requires a detailed treatment of the effects of the two dominant perturbations in the spectrum, viz. angular-radial coupling and Coriolis mixing. To illustrate the effects of these perturbations, we construct a trial basis set of stretching, internal rotor, and overall rotation functions,

$$\Psi^J(\alpha,\beta,\gamma,R,\theta,\phi)=\sum_{\Omega=-J}^{J}\sum_{j=0}^{j_{\max}}\sum_{k=-j}^{j}\sum_{n=0}^{n_{\max}}\chi_n(R)\times D^{J*}_{\Omega k}(0,\theta,\phi)D^{J*}_{M\Omega}(\gamma,\beta,\alpha). \quad (1)$$

Here, the functions $\chi_n(R)$ are approximate radial eigenfunctions and the D functions are normalized Wigner D matrices. The angles α,β,γ are the Euler angles necessary to specify the orientation of the complex in the laboratory frame of reference. To simplify the discussion below, this basis is transformed to a parity-adapted basis which diagonalizes the pure rotational Hamiltonian of water, and represented in Dirac notation,

$$|\Psi\rangle=\sum_{\Omega=0}^{J}\sum_{j_{k_ak_c}=0_{00}}^{j^{\max}}\sum_{n=0}^{n^{\max}}|n\rangle\left[\frac{2}{(1+\delta_{0\Omega})}\right]^{1/2}\times\{|j_{k_ak_c},\Omega\rangle|J\Omega\rangle+(-1)^{\epsilon}|j_{k_ak_c},-\Omega\rangle|J-\Omega\rangle\}. \quad (2)$$

This basis transforms as the irreducible representations (Γ) of the permutation-inversion group of the complex. If we express the angular momentum operators of the Hamiltonian in the basis of Eq. (2), then the rotational kinetic energy is given by a diagonal contribution

$$\frac{\hbar^2}{2\mu\mathbf{R}^2}[J(J+1)+j(j+1)-2\Omega^2]\delta_{\tau'\tau}\delta_{\Omega'\Omega}, \quad (3)$$

and an off-diagonal Coriolis term

$$\frac{\hbar^2}{2\mu\mathbf{R}^2}(C^{+}_{j\Omega}C^{+}_{J\Omega}+C^{-}_{j\Omega}C^{-}_{J\Omega})\delta_{\tau'\tau}\delta_{\Omega',\Omega\pm1}, \quad (4)$$

where

$$C^{\pm}_{j\Omega}=[j(j+1)-\Omega(\Omega\pm1)]^{1/2}.$$

Here, μ is the pseudodiatomic reduced mass, $\mathbf{R}$ the coordinate operator, and τ refers to all quantum numbers other than the projection quantum number (Ω) and the radial quantum number (n). As implied above, the Ω quantum number is nearly conserved if the Coriolis matrix element is small, since all other terms in the Hamiltonian, including the IPS, are diagonal in Ω. To further simplify the discussion, we shall neglect the effect of the operator $1/\mathbf{R}^2$ which, in principle, can mix different stretching basis functions. The additional constraint $\delta_{n,n'}$ can then be applied to Eqs. (3) and (4). The operator $\hbar^2/2\mu\mathbf{R}^2$ then represents purely inertial effects, and we replace it with its expectation value over the radial eigenfunction. This expectation value is represented by B, the rotational constant for the state in question. It is common to make an additional approximation, known as the reversed adiabatic approximation (RAA), viz. that all of the bending states in a given stretching manifold sample exactly the same effective radial surface. This amounts to a complete neglect of angular-radial coupling. A single rotational constant may then be associated with all states sharing the same radial quantum number. In what follows, we make the somewhat less restrictive approximation that all states associated with a given internal rotor level [e.g., Σ, Π, and $\Delta(2_{12})$] and stretching quantum number have the same rotational constant, but do not require that the states associated with different internal rotor levels [e.g., $\Sigma(1_{01})$ and $\Sigma(1_{11})$] sample an identical effective radial surface. We also assume that mixing between different free internal rotor states by the anisotropy in the IPS is insignificant. This last approximation is validated by full three-dimensional calculations[23] of the wave function which indicate that the individual internal rotor states are 95% pure in the absence of angular-radial coupling. However, it should be noted that this approximation does not hold for deuterated isotopes of water because of the smaller ratio of the rotational energy-level differences to the anisotropic terms in the potential-energy surface.

It is convenient to restrict our attention to states with total angular momentum $J=1$. In such states, only $\Omega=0$ (Σ) and $\Omega=1$ (Π) states are involved and the existence of $\Omega=2$ (Δ) states cannot yet complicate the picture. For a state having an internal rotor wave function dominated by $j=1$ (i.e., 1_{01}, 1_{11}, 1_{10}), the Coriolis matrix element reduces to

$$H_{\text{Coriolis}}=B[2j(j+1)J(J+1)]^{1/2}=2B[J(J+1)]^{1/2}, \quad (5)$$

while for $j=2$,

$$H_{\text{Coriolis}}=B[2j(j+1)J(J+1)]^{1/2}=2\sqrt{3}B[J(J+1)]^{1/2}. \quad (6)$$

A 2×2 Hamiltonian matrix for the mixed Σ^+ and Π^+ states results,

$$\begin{bmatrix} H_\Sigma & H_{\text{Coriolis}} \\ H_{\text{Coriolis}} & H_\pi \end{bmatrix}, \tag{7}$$

and the unperturbed component of the Π state which is of the opposite parity (denoted Π^-) has an energy

$$E_\pi^- = [H_\pi]. \tag{8}$$

The 2×2 matrix may be diagonalized perturbatively, assuming that $(H_{\text{Coriolis}})^2 \ll H_\Pi - H_\Sigma$, with the results,

$$E_{\Sigma^+} = H_\Sigma - H_{\text{Coriolis}^2}/(H_\Pi - H_\Sigma),$$
$$E_{\Pi^+} = H_\Pi + H_{\text{Coriolis}^2}/(H_\Pi - H_\Sigma). \tag{9}$$

Evaluating these expressions for $J=1$, the splitting between the two components of the Π state is shown to be approximately

$$E_{\Pi^+} - E_{\Pi^-} = 8B^2/(H_\Pi - H_\Sigma) \tag{10}$$

in states with $j=1$. The superscript plus-minus signs are used here solely to differentiate between the two components of the Π state and do not reflect any specific molecular symmetry.

In the fits to the experimental data presented below, we have tried to retain as much as possible of the form of rigorous Hamiltonian while allowing sufficient flexibility to reproduce the data to the measured accuracy. The diagonal VRT energies are expressed as a power-series expansion of Eq. (3), e.g.,

$$E = \nu + B[J(J+1) - 2\Omega^2] - D[J(J+1) - 2\Omega^2]^2$$
$$+ H[J(J+1) - 2\Omega^2]^3 + \cdots. \tag{11}$$

We include the factor of 2 multiplying Ω^2 in Eq. (3) in the expanded Hamiltonian [Eq. (11)]. This factor is not usually included in spectroscopic analysis, although it arises naturally in the expression of the Hamiltonian of the cluster in Jacobi coordinates. The difference is primarily formal, however, as it has a minor effect on the constants reported. We also include in the fits a parameter β which represents the effect of the portion of the off-diagonal Coriolis operator $\langle\tau,\Omega|\hbar^2/2\mu\mathbf{R}^2|\tau,\Omega\pm1\rangle$ which is not a simple function of the quantum numbers, j, J, and Ω. This treatment is a slight variation on our previous Coriolis analysis,[2] where we chose β to be equal to the entire coefficient multiplying $[J(J+1)]^{1/2}$.

Deviation of the parameter β from a value of $\beta=B$ should be interpreted as a breakdown of one or more of the approximations used to derive Eqs. (5) and (6). For instance, let us assume that the Π state in a Σ,Π internal rotor pair is a pure state and that the Σ state is mixed with other states (a common occurrence in $j=1$ of Rg–H_nX, X = F, Cl, Br, O, N). If the mixing is such that 50% of the Σ wave function is distributed over other states, then the effective value of β will be less than B. Specifically, it will be approximately equal to the product of the two coefficients C_Σ and C_Π, which describe the fraction of primitive wave function in the eigenstate, and B, i.e., $\beta = C_\Sigma \times C_\Pi \times B = 0.5\times1.0\times B$. The complete picture of the Coriolis interaction among the mixed states is more complex than this analysis suggests, since we must account for the effect of the other 50% of the Σ wave function on the l-type splitting in the Π state.

THE $j=1$ ORTHO STATES

The approximate treatment of Coriolis effects described above is remarkably accurate for the ortho $j=1$ VRT states of Ar–H_2O. The l splitting in $J=1$, $\Pi(1_{01})$ is measured to be 0.205 GHz. Substituting this value into Eq. (10), along with an approximate rotational constant $B=3.0$ GHz, yields an estimate of the energy difference between the $J=1$, $\Sigma(1_{01})$ level and the $J=1$, $\Pi(1_{01})$ state of 351 GHz. This compares to the experimental value of 340 GHz. In the $\Pi(1_{10})$ state, the observed splitting is 0.147 GHz, which yields an estimate of the spacing between $J=1$, $\Sigma(1_{10})$ and $J=1$, $\Pi(1_{10})$ of 489 GHz, compared to the experimental value of 452 GHz. In the 1_{01} states built upon one quantum of intermolecular stretch, the l-type splitting for $J=1$ is 0.181 GHz. Estimating the rotational constant in these two states to be 2.75 GHz, the splitting between the Σ and Π states is predicted to be 334 GHz, which is reasonable approximation to the experimentally observed splitting of 316 GHz. The more complete analysis of the Coriolis interaction from the least-squares fits to data spanning a range of angular momentum states supports the use of the approximations described in the above discussion of the dynamics of these states. The Coriolis parameter (β) determined in the fits nearly exactly equals B (within 5%) for all of the ortho $j=1$ levels states, as expected from the theoretical model developed above. This implies that the following three approximations are valid: (1) the angular wave functions are not strongly mixed, (2) there is not significant mixing of internal rotor and stretching levels due to angular-radial coupling, and (3) the kinetic-energy operator $1/R^2$ does not strongly mix different stretching states.

The results of a nonlinear least-squares fit of the measured VRT transitions to a model with a diagonal contribution to the Hamiltonian as given in Eq. (11) and an off-diagonal Coriolis term of $\beta[2j(j+1)J(J+1)]^{1/2}$ is presented in Table V. The rotational constants and the vibrational frequencies were constrained to be equal for both components of the Π states, but the effects of the distortion constants were not required to be identical for the two components. In Tables V–VII, constants which apply to only one component of an l-type doublet are identified by the symmetry of the $J=1$ level whose energy they describe. For example, $D(B_1)$ refers to the lower component of the l-type doublet in all three of the measured ortho $j=1$ Π states. The experimental data included in the analysis were the four rotational transitions in the $\Sigma(1_{01})$ state measured by Fraser *et al.*,[10] the combination difference from Lascola and Nesbitt,[12] which establishes the energy separation between $J=1$, $\Sigma(1_{01})$ and $J=1$, $B_2\Pi(1_{01})$ as 339763.(9) MHz, and 121 far-infrared VRT transitions. The FIR transitions include those reported by us previously,[1,2] and the new measurements of transitions to the $n=1$, $\Pi(1_{01})$ state. These new transitions range from $Q(1)$ to $Q(14)$ and from $P(4)$ to $R(0)$, and are shown along with the residuals from the fit in

TABLE V. Results of the least-squares fit to the $j = 1$ ortho Ar–H_2O transitions (MHz). The uncertainties in parentheses represent two standard deviations. The fit has an rms error (σ) of 0.623 MHz.

	$\Sigma(1_{01})$	$\Pi(1_{01})$	$\Pi(1_{10})$	$\Sigma(1_{10})$
ν	0	345 587.(18)	637 467.08(43)	1083 634.(18)
B	3014.783(27)	2951.658(57)	3037.476(15)	2953.224(66)
$D(B_1)$	0.072 616(71)	0.135 49(40)	0.060 44(13)	
$D(B_2)$		0.114 76(35)	0.051 42(14)	0.111 75(66)
$H(B_1)$	$1.25(20)\times10^{-6}$		$-2.145(28)\times10^{-5}$	
$H(B_2)$			$-1.238(32)\times10^{-5}$	$-2.39(22)\times10^{-5}$
β		2950.84(40)		2880.78(33)
	$n = 1, \Sigma(1_{01})$		$n = 1, \Pi(1_{01})$	
ν	1 019 239.27(70)		1 343 607.36(80)	
B	2 821.39(20)		2 693.670(50)	
$D(B_1)$	0.105 9(14)		0.211(29)	
$D(B_2)$			0.149 51(68)	
$H(B_1)$			$-1.01(22)\times10^{-5}$	
β		2683.6(37)		

Table I. The transitions were weighted by the inverse square of the experimental uncertainty: 4–5 kHz for the microwave transitions, 9 MHz for the infrared measurement, and 0.7 MHz for the far-infrared transitions. Transitions observed in previous work[1,2] are not reproduced here as they do not add significantly to the present discussion.

The rotation and distortion constants obtained for the $n = 0$, 1_{01} and 1_{10} states are essentially unchanged from the values which we presented in Ref. 2, and which have also been presented in Ref. 12. They are reproduced here primarily for purposes of comparison to the other states. In our previous analysis, β was totally correlated with the unknown separation between Σ and $\Pi(1_{01})$, which has since been measured by Lascola and Nesbitt.[12] As a result, the values here differ from those we presented in Ref. 2. Also, the rotational constant in the $n = 1$, $\Sigma(1_{01})$ state is significantly different from that reported previously, since we have now been able to decouple the effects of the Coriolis interaction on the rotational term values in that state by measurement of the $n = 1$, $\Pi(1_{01})$ VRT transition.

TABLE VI. Results of the least-squares fit to all available data for para Ar–H_2O (MHz).

(a)

	$\Sigma(0_{00})$	$n = 1, \Sigma(0_{00})$	$\Pi(1_{11})$	$\Sigma(1_{11})$
ν	0	907 322.59(61)	1 111 068.81(66)	1 219 866.16(75)
B	2988.286 39(45)	2867.402(35)	2994.813(14)	2830.12(13)
$D(A_2)$	0.096 324(73)	0.078 10(40)	0.3302(32)	$-0.0921(20)$
$D(A_1)$			0.094 129(92)	
$H(A_2)$		$-5.90(11)\times10^{-5}$	$-1.80(18)\times10^{-4}$	$2.36(12)\times10^{-4}$
β			2994.813 (fixed)	
C_{stretch}		0.40 (fixed)		
C_{bend}				0.704 63(26)
σ	1.5 MHz			

(b)

		Observed	Observed	Deperturbed rotational constants		
C_{stretch}	C_{bend}	$B[n=1, \Sigma(0_{00})]$	$B[\Sigma(1_{11})]$	$B[n=1, \Sigma(0_{00})]$	$B[\Sigma(1_{11})]$	$B[\Sigma(?)]$
0.2	0.6535	2845.6	2851.7	2839.0	2995.0	2731.0
0.3	0.6753	2854.7	2842.7	2840.0	2995.0	2681.0
0.4	0.7046	2867.4	2830.1	2842.0	2995.0	2571.0
0.5	0.7406	2883.8	2813.9	2845.0	2995.0	2236.0
0.6	0.7824	2903.8	2794.2	2849.0	2827.0	...

TABLE VII. Results of two different least squares fits to the $\Sigma,\Pi(2_{12})\leftarrow\Sigma(1_{01})$ bands. The differences between the fits are discussed in the text.

(a)

	$\Sigma(2_{12})$ $[B_1]$	$\Pi(2_{12})$ $[B_2]$ (Q branch)	$\Pi(2_{12})$ $[B_1]$ (P and R branches)
ν	1 684 904.7(90)	1 840 071.3(13)	1 840 743.6(13)
B	2 522.99(11)	2 827.98(10)	3 156.03(38)
D	0 (fixed)	0.026 8(20)	2.908(28)
H	0 (fixed)	$-3.3(12)\times10^{-5}$	0.011 37(82)
L	0 (fixed)	$-3.72(28)\times10^{-7}$	$-5.64(92)\times10^{-5}$
M	0 (fixed)	0 (fixed)	$-1.49(34)\times10^{-7}$
σ	0.98 MHz (13 parameters)		

(b)

	$\Sigma(2_{12})$ $[B_1]$	$\Pi(2_{12})$ $[B_2]$ (Q branch)	$\Pi(2_{12})$ $[B_1]$ (P and R branches)
ν	1 684 206.1(11)	1 840 078.21(98)	1 840 078.21(fixed)
B	2 848.39(24)	2 827.555(85)	2 827.555(fixed)
D	0 (fixed)	0.019 9(17)	2.238 1(85)
H	0 (fixed)	$-7.3(12)\times10^{-5}$	0.003 58(13)
L	0 (fixed)	$-2.95(26)\times10^{-7}$	$-1.1(66)\times10^{-5}$
β	2 037.24(46)		
σ	2.8 MHz (11 parameters)		

THE PARA STATES

In the Σ and $\Pi(1_{11})$ internal rotor levels of Ar–H_2O, a severe breakdown of the approximations described above and used to accurately interpret the effect of the Coriolis operator on the $j=1$ ortho states of Ar–H_2O is observed. For example, we measure the l-type splitting in $J=1$, $\Pi(1_{11})$ to be 0.251 GHz. Substituting an approximate rotational constant of 3.0 GHz into Eq. (10), along with the l-type splitting, the $\Pi(1_{11})$ state is predicted to be 286 GHz lower in energy than the $\Sigma(1_{11})$ state. This is more than twice the experimentally measured spacing of 115 GHz. Note also [Eqs. (9) and (10)] that the Coriolis-induced shift in the rotational term value of $J=1$ in the Σ level is equal to the splitting in the Π state. Inspection of Table IV shows that the errors in the 1_{11} term values are not equal. The energy of $J=1$ $A_2\Sigma(1_{11})$ is predicted 215 MHz too high, but $J=1$ $A_2\Pi(1_{11})$ is predicted only 111 MHz too low. Furthermore, less than 50% of the difference between the predicted and the measured l-type splittings can be accounted for by the difference between the measured and predicted spacing of the $\Sigma(1_{11})$ and $\Pi(1_{11})$ states. Using the measured spacing of these two VRT states (115 GHz) and Eq. (10), one can correct the prediction obtained from the AW1 surface of (362 MHz) to get a new estimate for the l-type splitting in $J=1$ of the Π state of 315 MHz. This is still 60 MHz greater than the measured value of 253 MHz. This difference alone can be interpreted as a clear indication that one or both of the states involved in the Coriolis interaction is not a pure state but is substantially mixed. Further evidence is obtained from a corrected estimate of the $J=1\leftarrow0$ term value in $\Sigma(1_{11})$. For this transition, correcting for the difference between the measured and the observed position of $\Sigma(1_{11})$ gives an adjusted estimate of 6129 MHz. This is still more than 150 MHz from the experimental value of 5971.1 MHz. In addition to the Coriolis effects, there must be interactions which cause the effective rotational energy of $J=1$ $A_2\Sigma(1_{11})$ to be smaller than predicted on the AW1 surface. We believe this discrepancy to be caused by angular-radial coupling in the IPS which mixes $\Sigma(1_{11})$ with $n=1$, $\Sigma(0_{00})$ and perhaps other states, for the following reasons. (1) No reasonable effective angular potential derived by neglecting angular-radial coupling reproduces the observed ortho and para $j=1$ VRT energies. Specifically, $\Sigma(1_{11})$ is always predicted to lie *below* $\Pi(1_{11})$ on surfaces which reproduce the ortho splittings, although it is observed *above* it. (2) In our discussion of the IPS of Ar–H_2O in Ref. 3, we pointed out the $\Sigma(1_{11})$ state of Ar–H_2O is strongly affected by anisotropy in the position of the radial minimum, an effect primarily resulting from anisotropy in the repulsive wall. (3) The $n=1$, $\Sigma(0_{00})\leftarrow n=0$, $\Sigma(0_{00})$ stretching band is observed to be 3.4 cm^{-1} below the $n=1$, $\Sigma(1_{01})\leftarrow n=0$, $\Sigma(1_{01})$ stretching band. This large difference suggests that one or both of these stretching states is interacting strongly with a nearby internal rotor level, and/or that they sample drastically different effective radial potentials. (4) The difference between the predicted and observed rotational term values in the $\Sigma(1_{11})$ state can be accounted for by coupling to a state with a much smaller effective rotational constant, such as an excited stretching state. (5) Full three-dimensional calculations of the wave functions on the AW1 surface unambiguously demonstrate that in Ar–H_2O the $\Sigma(1_{11})$ is strongly mixed with $n=1$, $\Sigma(0_{00})$.

The experimental data for the three para levels of Ar–H_2O were included in a simultaneous weighted least-squares fit. These include new lines ranging from $Q(1)$–$Q(16)$ and $P(12)$–$R(7)$ in the $\Pi(1_{11})$–$\Sigma(0_{00})$ band, from $P(11)$ to $R(8)$ in the $\Sigma(1_{11})$–$\Sigma(0_{00})$ band, and the previously measured[2] transitions ranging from $P(5)$ to $R(14)$ in the $n=1$, $\Sigma(0_{00})$–$\Sigma(0_{00})$ band. The microwave transitions observed by Fraser *et al.*[10] were also included, weighted by the reported measurement uncertainty. The far-infrared transitions were given a weight of 0.7 MHz, except for lines in the P and R branches of $\Pi(1_{11})\leftarrow\Sigma(0_{00})$, for which there is an apparent systematic error of 1–2 MHz in the measurements. These were assigned an uncertainty of 2.0 MHz. As for the ortho levels, we have fit the observed frequencies to a model Hamiltonian consisting of diagonal energies [Eq. (11)] and an off-diagonal Coriolis mixing term. A 3×3 matrix is constructed for these states as shown in Eq. (12),

$$\begin{bmatrix} H_{\text{stretch}} & C_{\text{stretch}}H_{\text{Coriolis}} & 0 \\ C_{\text{stretch}}H_{\text{Coriolis}} & H_{\Pi} & C_{\text{bend}}H_{\text{Coriolis}} \\ 0 & C_{\text{bend}}H_{\text{Coriolis}} & H_{\Sigma} \end{bmatrix},$$

$$H_{\text{Coriolis}}=\beta\sqrt{2j(j+1)J(J+1)}. \tag{12}$$

The Coriolis operator is assumed to connect both the $n=1$, $\Sigma(0_{00})$ and the $\Sigma(1_{11})$ states to the $\Pi(1_{11})$ state. We also assume that the Π state is not significantly mixed with other states, viz. $C_{\Pi}=1.0$. The off-diagonal matrix element con-

necting $n=1$, $\Sigma(0_{00})$ to $\Pi(1_{11})$ is set equal to C_{stretch} (H_{Coriolis}), and that connecting $\Sigma(1_{11})$ to $\Pi(1_{11})$ is equal to C_{bend} (H_{Coriolis}). Contributions to the Coriolis effects from other states are expected to be small. Since the nearest Σ eigenstate is about 20 cm^{-1} away from the Π state (Fig. 4), the energy denominator causes Coriolis effects from interaction with these states to be at least six times smaller than from interaction with $\Sigma(1_{11})$ or $n=1, \Sigma(0_{00})$. The contribution is further reduced by the small coefficient of $\Sigma(1_{11})$ in the other eigenstates [most of this basis state is contained in the $\Sigma(1_{11})$ eigenstate]. Analysis of the rotational term values presented below demonstrates that at least one other state is involved in the coupling to $\Sigma(1_{11})$. Accordingly, we did not constrain the sum of C^2_{stretch} and C^2_{bend} to be equal to one. Attempts to simultaneously determine both of these coefficients and the Coriolis constant (β) led to fits which were too highly correlated to be considered useful. Accordingly, we fixed the Coriolis constant to be approximately the rotational constant of the $\Pi(1_{11})$ state. This approximation is expected to be accurate to a few percent based on the results for the ortho $j=1$ levels where B and β were within 5% of each other. We then fit the coefficient describing the amount (C_{bend}) of the primitive basis function $\Sigma(1_{11})$ in the $\Sigma(1_{11})$ eigenstate, fixing the coefficient (C_{stretch}) describing the quantity of this basis function mixed into the $n=1, \Sigma(0_{00})$ eigenstate at a series of different values. The fits were found to be strongly sensitive to the quantity C_{bend}, but fits with the mixing coefficient C_{stretch} fixed anywhere in the range from 0–0.6, all had rms errors that are consistent with the experimental uncertainty, and give $C^2_{\text{bend}} + C^2_{\text{stretch}} < 1.0$. The fit obtained with C_{stretch} fixed at 0.4 is shown in Table VI(a), and the residuals from this fit are shown in Table II. In Table VI(b) we also give values of C_{bend} and the rotational constants for the $n=1, \Sigma(0_{00})$ and the $n=0, \Sigma(1_{11})$ eigenstates, obtained from fits with C_{stretch} fixed in the range 0.2–0.6. Over this range of C_{stretch}, the C_{bend} coefficient was found to vary from 0.66 to 0.79. The comparatively narrow range results because the Σ and $\Pi(1_{11})$ states are a factor of 2 closer to each other than the $\Pi(1_{11})$ state is to the $n=1, \Sigma(0_{00})$ state. The interaction between the two 1_{11} states thus dominates the l-type splitting in the Π state, which in turn, determines the value of C_{bend}.

The extensive mixing of the two Σ levels with each other and with other states makes it more difficult to specify the deperturbed rotational constants of the para basis states than for the ortho $j=1$ basis states. If we assume (1) the $n=1$, $\Sigma(0_{00})$ eigenstate consists only of $\Sigma(1_{11})$ and $n=1, \Sigma(0_{00})$ basis states, and (2) the rotational constant in the unperturbed $\Sigma(1_{11})$ basis state is equal to that in the $\Pi(1_{11})$ state [$B^{[\Sigma(1_{11})]}_{\text{fixed}} = 2994.813(44)$ MHz], then we can derive the rotational constants for the unperturbed basis states, including that of a third unknown state which is mixed into $\Sigma(1_{11})$. The necessary relationships are given in Eq. (13),

$$B^{[n=1,\ \Sigma(0_{00})]}_{\text{observed}} = (1.0 - C^2_{\text{stretch}})B^{[n=1,\ \Sigma(0_{00})]} + (C^2_{\text{stretch}})B^{[\Sigma(1_{11})]}_{\text{fixed}},$$

$$B^{[n=0,\ \Sigma(1_{11})]}_{\text{observed}} = (C^2_{\text{stretch}})B^{[n=1,\ \Sigma(0_{00})]} + (C^2_{\text{bend}})B^{[\Sigma(1_{11})]}_{\text{fixed}} + (1.0 - C^2_{\text{stretch}} - C^2_{\text{bend}})B^{*}. \quad (13)$$

Here, C_{bend}, C_{stretch}, and the observed rotational constants are taken from Table VI(b), and we solve for the two unknowns $B^{[n=1,\ \Sigma(0_{00})]}$ and B^{*}. The deperturbed rotational constants are shown in Table VI. For C_{stretch} fixed at 0.6, Eq. (13) produces a negative rotational constant for the third state. For this value of C_{stretch}, we relax the second assumption and allow the rotational constant of $\Sigma(1_{11})$ to be different from that of $\Pi(1_{11})$ and assume the interaction may be explained entirely by mixing of the two measured Σ states. This analysis gives $B[n=1,\ \Sigma(0_{00})] = 2849.0$ MHz and $B[\Sigma(1_{11})] = 2827.0$ MHz. These rotational constants imply an average bond length in the internal rotor state which is larger than in the stretching fundamental. This is a physically unreasonable result. A more appropriate inference is that this value of the coupling constant, $C_{\text{stretch}} = 0.6$, is too high. Over the range, $C_{\text{stretch}} = 0.2$–0.5, we find the $n=1, \Sigma(0_{00})$ rotational constant to range from 2839.0–284.0 MHz. This is within 30 MHz of the value of B in the $n=1, \Sigma(1_{01})$ state, 2821.24(44) MHz, which we interpret as support for this deperturbation model. However, it is not likely that the rotational constant of $\Sigma(1_{11})$ is exactly 2995 MHz. Allowing the rotational constant for $\Sigma(1_{11})$ to be smaller than 2995 MHz would drive the rotational constant of the excited stretching state to higher values; allowing it to be larger than 2995 MHz would decrease its value. The latter is more likely, since two-dimensional angular surfaces[3] indicate the $\Sigma(1_{11})$ state is stabilized by the IPS more than is the $\Pi(1_{11})$ state, and since that would bring the rotational constant in the 0_{00} stretch closer to the values in the 1_{01} stretching levels.

The coefficients which determine the wave functions of the $n=1, \Sigma(0_{00})$ and the $\Sigma(1_{11})$ states may be inverted to obtain the size of the angular-radial coupling matrix element and the deperturbed frequencies of the two states. Neglecting the contributions from the third perturbing state, we find $H_{\text{angular-radial}}$ is 5 cm^{-1} for $C_{\text{stretch}} = 0.6$ and it is 3 cm^{-1} for $C_{\text{stretch}} = 0.3$. The corresponding deperturbed frequencies for $n=1, \Sigma(0_{00})$ are 1020 or 935 GHz for $C_{\text{stretch}} = 0.6$ and 0.3, respectively. The deperturbed frequencies of $\Sigma(1_{11})$ are 1108 and 1191 GHz, respectively. At $C_{\text{stretch}} = 0.6$, the value for the deperturbed stretching frequency is nearly identical to the frequency of the stretches built on the Σ and $\Pi(1_{01})$ states, which are 1019 and 998 GHz, respectively. This suggests that the coupling matrix element mixing these two states is nearly the strongest that is consistent with the rotational constants, $C_{\text{stretch}} = 0.5$–0.6. The 1108 GHz value for $\Sigma(1_{11})$ is also close to the value predicted by purely angular models.[3] This lends additional support to the model for the deperturbation and to the conclusion that the mixing is strong.

THE 2_{12} STATES

Analysis of the Coriolis effects on the $\Pi(2_{12})$ state rotational term values clearly evidences the presence of either strong angular-radial coupling or of strong mixing with other internal rotor states. Since angular-radial coupling has

already been shown to have a strong effect on the para states, and because no significant mixing of Σ or $\Pi(2_{12})$ with other internal rotor states is indicated using effective angular potential surfaces, we assume that additional angular-radial coupling beyond that present in the AW1 surface is responsible for the differences between the observed l-type splittings and those calculated on the AW1 surface. For $J=1$ states in a $j=2$ internal rotor level the Coriolis matrix element is given in Eq. (6). Solving the 2×2 matrix for the $J=1$ Σ and $\Pi(2_{12})$ energies perturbatively gives a splitting in $J=1$ of $24B^2/\Delta E$ in the Π state, where ΔE is the energy spacing of the Σ and Π levels. Using the measured l-type splitting in $J=1$, 0.672 GHz, and approximating the rotational constant to be 3.0 GHz, we find $\Delta E=321$ GHz, which is more than twice the measured value of 150(10) GHz.

VRT state mixing in the 2_{12} states is much more complex than in the 1_{11} states. The $n=2$, $\Sigma(1_{01})$ stretching level most likely dominates the perturbation, mixing strongly with $\Sigma(2_{12})$. The $\Pi(2_{12})$ state has two nearby Π stretching levels which it may interact with $n=1$, $\Pi(1_{10})$ and $n=2$, $\Pi(1_{01})$. For $J>1$, the effects of the Coriolis interaction with the $\Delta(2_{12})$ state must also be taken into account. In addition to these complications, the experimental data set is not as complete. None of the perturbing states has been observed, preventing a characterization of the mixing at the level of detail that was presented for the para levels. Also, only a few lines in the $\Sigma(2_{12})\leftarrow\Sigma(1_{01})$ band have been assigned. We have measured a series of strong transitions in the range 1690–1706 GHz which we believe are the R branch of $\Sigma(2_{12})$. All of these lines were easily observed on the second sideband ($\nu_{\text{laser}}\pm2\nu_{\text{microwaves}}$) from both the 1757 and the 1626 GHz laser lines. This gives an indication of their exceptionally large intensities. The $P(10)$, $P(9)$, $R(7)$, and $R(8)$ lines have been assigned based on lower state combination differences. Other P-branch lines are either obscured by atmospheric water, which is especially problematic in this region, and/or are in regions where the available microwave sources do not provide sufficient power to observe them. It is also likely that the P branch is much less intense than the R branch because of the intensity perturbations caused by the strong Coriolis mixing. In the limit of very strong Coriolis mixing, the transitions to the P branch become forbidden altogether. In this limit the internal angular momentum (j) and the overall angular momentum (l) are both nearly good quantum numbers. The P-branch transitions correspond to electric dipole forbidden $\Delta l=2$, $\Delta j=1$ transitions and the R branch to allowed $\Delta l=0$, $\Delta j=1$ transitions. The strong Coriolis perturbation also causes the R-branch pattern to be highly irregular, with a bandhead at $R(4)$ or $R(5)$, and prevents accurate estimates of the line positions even for the transitions adjacent to those which have been assigned, without a more accurate treatment of the Coriolis interactions than is currently possible. The lines are assigned to the $\Sigma(2_{12})\leftarrow\Sigma(1_{01})$ band based on their intensity, approximate position, and the rotational term values which are consistent with expectations for this strongly mixed band. The only other band expected in this region is $n=1$, $\Pi(1_{10})\leftarrow\Sigma(1_{01})$, which is expected to be much weaker and not to display as strong a Coriolis perturbation to the rotation term values as is evident in the $\Sigma(2_{12})\leftarrow\Sigma(1_{01})$ band.

In Table VII, we present two fits to the four assigned $\Sigma(2_{12})\leftarrow\Sigma(1_{01})$ transitions and the $\Pi(2_{12})\leftarrow\Sigma(1_{01})$ transitions, including lines ranging from $P(11)$–$R(9)$ and $Q(1)$–$Q(15)$. The ground-state $\Sigma(1_{01})$ constants were held fixed at the results from the fit discussed above and presented in Table V. In the first fit (a) we modeled each state separately using the Hamiltonian of Eq. (11) and omitted the obviously strong Coriolis coupling. The two components of the Π state are treated separately in this fit. Predictions of the positions of the $\Sigma(2_{12})$ R branch transitions based on this fit are consistent with the assignment of the strong lines in the 1690–1705 region to this band. In the second fit (b) the two observed 2_{12} states were assumed to be coupled by a Coriolis matrix element of the form given in Eq. (6). However, the actual quantity $\beta=2037.24(46)$ MHz, determined in the fit, should be interpreted as $C_\Sigma\times C_\Pi\times\beta'$, where β' is the expectation value of the operator $\hbar^2/2\mu R^2$ between the two states. If we assume that the value of β' ranges from 2850 to 3000 MHz, then the product, $C_\Sigma\times C_\Pi$, ranges from 0.71 to 0.68. This indicates that the mixing in the 2_{12} levels is comparable to that in the 1_{11} levels, for which C_Σ was determined to range from 0.65 to 0.69 and C_Π was assumed to be 1.0. The actual mixing may be somewhat smaller than this analysis indicates. The $n=2$, $\Sigma(1_{01})$ level pushes the perturbed component of the $\Pi(2_{12})$ state in the opposite direction from the $\Sigma(2_{12})$ state. Since the $n=2$, $\Sigma(1_{01})$ state is closer to $\Pi(2_{12})$ than $\Pi(2_{12})$ is to $\Sigma(2_{12})$, the effects of Coriolis coupling to $n=2$, $\Sigma(1_{01})$ are large. By $J=13$ the larger rotational constant of the $\Pi(2_{12})$ state compared to $n=2$, $\Sigma(1_{01})$ reduces the energy denominator in the interaction with this stretching level sufficiently that the effect of the two Coriolis interactions are nearly equal but in opposite directions. At this value of J the l-type splitting approaches zero. A full analysis including the effects of the $n=2$, $\Sigma(1_{01})$ stretching state would give a larger Coriolis constant to compensate for the additional perturbation, and hence a larger value for the product $C_\Sigma\times C_\Pi$. More detailed treatment of the spectra than that presented here will require measurement of the $n=2$, Σ and $\Pi(1_{01})$ levels, and the $n=1$, $\Pi(1_{10})$ and the $\Delta(2_{12})$ state, so that the effects of coupling to these states can be treated explicitly. Alternatively, a direct fit to the three-dimensional IPS should reveal the nature of the VRT mixing in these states in great detail.

DISCUSSION

Twelve VRT states of Ar–H_2O, including the five new states described in this paper, have now been characterized by TFIR laser spectroscopy. A detailed analysis of the changes required in the AW1 IPS by these and other recently acquired data will be presented in a forthcoming paper,[23] in which a direct fit of the data to a new model for the three-dimensional IPS is presented. It is nevertheless very useful to attempt to gain qualitative insight into the relationship between the structure of the IPS, the intermolecular dynamics on that surface, and the VRT spectra, particularly since the full three-dimensional calculations are expensive and time

consuming. In Fig. 8, we present a pictorial description of the internal motion and the most probable orientation of the H_2O subunit within the complex for each of the six $j=1$ internal rotor states. It is useful to think of the orientational distribution of the internal rotor levels as being analogous to that of electrons in atomic orbitals. The $j=0$ level is like an s orbital and samples essentially all orientations with equal probability, the $j=1$ internal rotor functions are analogous to p orbitals, the $j=2$ to d orbitals, etc. This model is similar to those which have been presented for atom–diatom clusters.[24,25] However, water is an asymmetric rotor and has much more complex internal dynamics within a cluster than does a linear molecule. The three $j=1$ levels of water each have the projection of the H_2O angular momentum along a different inertial axis. The 1_{01} state rotates about the c axis, which is perpendicular to the molecular plane; 1_{11} rotates about the b axis, which is the C_{2v} symmetry axis; and 1_{10} rotates about the a axis. Each of these states can rotate with its angular momentum quantized along the van der Waals bond. In the $j=1$ levels, the molecule is in a Σ state when the axis of rotation is perpendicular to the van der Waals bond axis; and when the axis of rotation is along the van der Waals bond, the molecule is in a Π state. The orientational distributions indicated pictorially in Fig. 8 are also summarized in Table VIII.

The effects of the IPS on these states can be predicted directly from inspection of Figs. 2 and 8. The $\Sigma(1_{01})$ state is observed at lower energy than the $\Pi(1_{01})$ state, since $\Pi(1_{01})$ is localized at $\theta=90°$, $\phi=90°$, the position of the largest barrier to internal rotation (47 cm^{-1}). Similarly, $\Pi(1_{10})$ is localized near the global minimum at $\theta=90°$, $\phi=0°$; as a result it is lower in energy than the $\Sigma(1_{01})$ state,

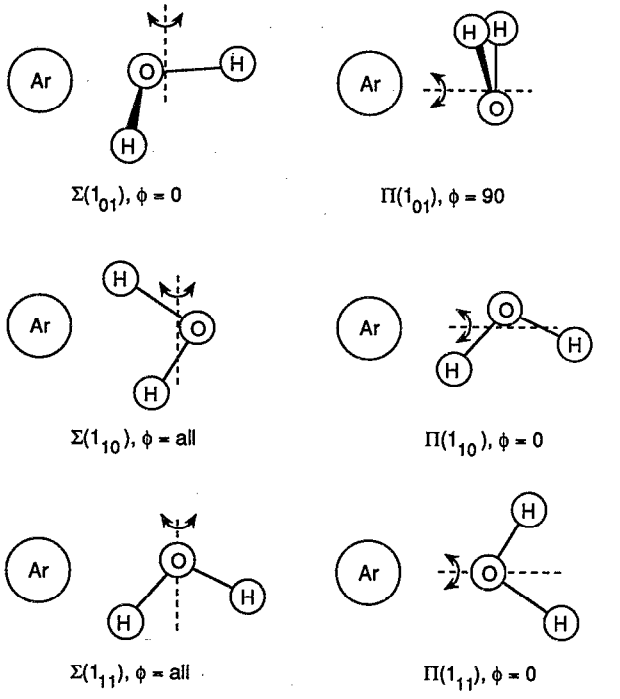

FIG. 8. A pictorial representation of the $j=1$ internal rotor states of Ar–H_2O.

TABLE VIII. Orientations and average radial distances of the observed Ar–H_2O states.

State	Orientation	$\langle\|R\|\rangle$ (Å)
$\Sigma(0_{00})$	isotropic	3.691
$\Sigma(1_{01})$	$\theta=$ all, $\phi=0°$	3.674
$\Pi(1_{01})$	$\theta=90°$, $\phi=90°$	3.714
$\Pi(1_{10})$	$\theta=90°$, $\phi=0°$	3.661
$\Sigma(1_{10})$	$\theta=$ all, $\phi=$ all	3.713
	(maintains C_{2v} symmetry during the rotation)	
$\Pi(1_{11})$	$\theta=0°$ or 180°, $\phi=0°$	3.718
$\Sigma(1_{11})$	$\theta=90°$, $\phi=$ all	3.778
$n=1$, $\Sigma(0_{00})$	isotropic	3.782
$n=1$, $\Sigma(1_{01})$	$\theta=$ all, $\phi=0°$	3.798
$n=1$, $\Pi(1_{01})$	$\theta=90°$, $\phi=90°$	3.887
$\Sigma(2_{12})$		3.78–4.01
$\Pi(2_{12})$		3.794
Deperturbed values		
$\Sigma(1_{11})$	$\theta=90$, $\phi=$ all	3.718 (fixed)
$n=1$, $\Sigma(0_{00})$	isotropic	3.787–3.807
$\Sigma(?)$		3.948–4.285

which has amplitude at both barriers to in-plane rotation (22 and 17 cm^{-1}) and at the barrier to out-of-plane rotation, but has a node at the global minimum. Both 1_{11} states have significant amplitude at the barriers; $\Pi(1_{11})$ samples at the barriers to in-plane rotation, and $\Sigma(1_{11})$ samples both at the maximum barrier to out-of-plane motion and at the global minimum. The analysis of the VRT dynamics in the two angular coordinates presented by Hutson[4] shows that $\Sigma(1_{11})$ is more stable, but this result is not obvious upon inspection of the IPS.

In addition to the nominal orientations of the water monomer in the different states, the average radial distance obtained by treating the water as a point mass and inverting the rotational constants from Tables V–VII is summarized in Table VIII. In every case, the average bond length of the state in a Σ,Π pair which samples the barriers is longer than the bond length of the state which samples near the minimum. The average bond length in the $n=0, j=0$, and $j=1$ states ranges from 3.67 to 3.72 Å. In $n=1$, it is 3.78–3.89 Å. From Fig. 1, the repulsive anisotropy at the zero of energy on the AW1 IPS can be seen to be about 0.17 Å, with the argon able to approach to 2.9 Å near the oxygen atom, but only to within 3.07 Å near the hydrogen atoms. The observed states sample much lower on the repulsive wall, and have a variation in bond length which is consistent with a smaller repulsive anisotropy near the minimum, 0.05 Å in $n=0$, and 0.1 Å in $n=1$. The $n=0$, $\Pi(2_{12})$ state has an average bond distance of 3.81 Å. This is too large for a state which is purely $n=0$. Since this state is dominated by an $n=0$ internal rotor state, it must be mixed with a state that has a bond length which is on average much longer than 3.8 Å, most likely $n=2$, $\Pi(1_{01})$.

CONCLUSIONS

The spectra presented in this paper provide strong evidence for angular-radial coupling as one of the dominant

features of the IPS of Ar–H_2O, especially in the vicinity of the potential minimum. These measurements will provide the basis for the determination of a substantially more accurate IPS for Ar–H_2O than is currently available. We also describe a simple and complete formalism for the analysis of Coriolis effects in the VRT spectra of any weakly or moderately anisotropic atom–molecule complex. This formalism can be used to test the accuracy of the commonly employed reversed adiabatic approximation and to establish a quantitative description of the angular-radial coupling in the IPS of the complex in question.

It is informative to apply this analytical framework for a comparison of the spectra and experimental IPS's among the first-row hydrides Ar–HF($v=1$),[25,26] Ar–H_2O,[1–3] and Ar–NH_3.[27,28] In both Ar–H_2O and Ar–NH_3, there is substantial experimental evidence for strong angular-radial coupling, but no such evidence has been presented for Ar–HF($v=1$).[25] The Ar–HF($v=1$) IPS determined by Nesbitt, Child, and Clary,[26] through inversion of extensive midinfrared spectroscopic data, exhibits only a weak variation in the position of the radial minimum as a function of the angle of the interaction, viz. in the linear Ar–HF and Ar–FH configurations, the minimum is located at 3.40 Å, while at the barrier to internal rotation at 90°, the minimum occurs at 3.55 Å. Whether this should be interpreted to imply that the angular-radial coupling is genuinely small in this complex, or that the spectroscopic data set used to develop this surface is simply not an accurate probe of these features of the surface, is an interesting question. For both Ar–NH_3 and Ar–H_2O, internal rotor and stretching levels have been observed which, in the absence of angular-radial coupling, would be nearly degenerate. The strong interaction between the internal rotor and stretching levels that is reflected in these experimental observables (band positions, hyperfine matrix element, l-type splittings) provides a precise measure of the coupling matrix elements. However, in Ar–HF the observed bending and stretching levels that could potentially be mixed by an angular-radial coupling matrix element are all more than 10 cm^{-1} apart. This spacing is considerably larger than the angular-radial coupling matrix element, which is on the order of 3–5 cm^{-1} in Ar–H_2O and Ar–NH_3. Hence, angular-radial coupling would be much harder to detect in the band positions of the particular states sampled by the mid-infrared experiments, even if this were a dominant feature of the IPS. However, the l-type splittings are more sensitive to the effects of angular-radial coupling. In fact, the most significant discrepancies (5%–25%) between predictions using the Ar–HF($v=1$) surface obtained by Nesbitt, Child, and Clary[26] and the experimental data obtained by Lovejoy and Nesbitt[25] are associated with l-type splittings. It thus seems likely that the IPS of Ref. 26 underestimates the importance of angular-radial coupling, a fact which Nesbitt, Child, and Clary[26] specifically acknowledge, although claiming it to be a minor inadequacy.

In the Rg–HX complexes, angular-radial coupling is primarily the result of the difference in the van der Waals bond lengths at the Rg–HX and Rg–XH configurations. Because of the importance of angular-radial coupling in clusters of argon with other molecules, it will be important to develop a more quantitative assessment of the position of the potential minima in Ar–HF. As Hutson points out,[24] the electron withdrawing effect of the hydrogen atom reduces the repulsion at the Rg–XH geometry, giving rise to the secondary minimum at this structure at a shorter intermolecular spacing than at the Rg–HX geometry. This effect becomes increasingly important as the size of the halogen atom is increased and as electronegativity decreases, in the series Ar–HF, Ar–HCl, and Ar–HBr. For this reason, angular-radial coupling is expected to be weakest, and therefore difficult to detect in Ar–HF. It will be interesting to make a comparison of the potentials for the first-row hydrides so as to understand the trend toward increasing angular-radial coupling from Ar–HF to Ar–NH_3.

The other question which these data raise is: What is the *source* of the angular-radial coupling itself? Angular-radial coupling must become important at some distance if there is any anisotropy at the potential minimum. At long range, this anisotropy must go smoothly to zero. In an atom–molecule complex, the induction forces are small, and the anisotropy is largely determined by the balance between exponential repulsive forces and attractive dispersion forces. The repulsive forces are rapidly varying in the region of the minimum, while the long-range dispersion forces are changing more slowly. Examination of the different contributions to the AW1 IPS (Ref. 3) indicates that the dominant contribution to angular-radial coupling results from anisotropy in the repulsive wall. This anisotropy changes nearly twice as fast as the attractive anisotropies over the range 3.6–4.0 Å. van Bladel and Van der Avoird[29] make a similar argument for repulsive anisotropy in the VRT spectra of Ar–NH_3 based on their computed wave functions and energies on the *ab initio* surface of Bulski, Wormer, and Van der Avoird.[30] These authors find that the most significant anisotropy in the region of the minimum is due to short-range repulsive forces. Experimental manifestations of angular-radial coupling in Ar–NH_3 have been discussed by Schmuttenmaer *et al.*,[27] who also concluded that FIR VRT spectra demand that significant anisotropic repulsive forces contribute in the region of the minimum on the Ar–NH_3 IPS.

In summary, five new VRT states of Ar–H_2O have been measured and analyzed. These states significantly expand the database available for determination of the Ar–H_2O IPS. States with energies up to 65% of the AW1 dissociation limit, $D_e = 174.7$ cm^{-1} have now been observed. These states sample the full range of the angular degrees of freedom. In the radial degree of freedom, the states span a range of average center-of-mass separations from 3.66 to 3.89 Å. The $n=2$ stretching levels have been accessed indirectly through perturbations. They have an average bond length exceeding 3.95 Å. Finally, not only do these spectra sample an extended range of intermolecular coordinates, but they provide a precise probe of the van der Waals bond length as a function of orientation (angular-radial coupling) in the IPS.

ACKNOWLEDGMENTS

The authors acknowledge helpful discussions with C. A. Schmuttenmaer and assistance with some of the experiments

described in this work from D. W. Steyert and M. J. Elrod. We thank Professor David Nesbitt for communicating his near-IR results to us before publication. This work was funded by the Experimental Physical Chemistry Program of the National Science Foundation (Grant No. CHE-8612296). R.C.C. was supported by the Director, Office of Energy Research, Office of Basic Energy Sciences, Chemical Sciences Division of the U.S. Department of Energy, under Contract No. DE-AC03-76SF00098.

[1] R. C. Cohen, K. L. Busarow, K. B. Laughlin, G. A. Blake, M. Havenith, Y. T. Lee, and R. J. Saykally, J. Chem. Phys. **89**, 4494 (1988).
[2] R. C. Cohen, K. L. Busarow, Y. T. Lee, and R. J. Saykally, J. Chem. Phys. **92**, 169 (1990).
[3] R. C. Cohen and R. J. Saykally, J. Phys. Chem. **94**, 7991 (1990).
[4] J. M. Hutson, J. Chem. Phys. **92**, 157 (1990).
[5] W. Yang and A. C. Peet, Chem. Phys. Lett. **153**, 98 (1988).
[6] A. C. Peet and W. Yang, J. Chem. Phys. **90**, 1746 (1989).
[7] A. C. Peet and W. Yang, J. Chem. Phys. **91**, 6598 (1989).
[8] W. Yang and A. C. Peet, J. Chem. Phys. **92**, 522 (1990).
[9] J. M. Hutson, Annu. Rev. Phys. Chem. **41**, 123 (1990).
[10] G. T. Fraser, F. J. Lovas, R. D. Suenram, and K. T. Matsumura, J. Mol. Spectrosc. **144**, 97 (1990).
[11] H. Gutowsky and T. C. Germann (private communication).
[12] R. Lascola and D. J. Nesbitt, J. Chem. Phys. (submitted).
[13] S. Suzuki, R. E. Bumgarner, P. A. Stockman, P. G. Green, and G. A. Blake, J. Chem. Phys. **94**, 824 (1991).
[14] E. Zwart and W. L. Meerts, Chem. Phys. **151**, 407 (1991).
[15] S. Green, J. Chem. Phys. **95**, 3888 (1991).
[16] J. R. Rusk, J. Chem. Phys. **42**, 493 (1965); A. Bauer, M. Godon, M. Kheddar, J. M. Hartmann, J. Bonamy, and D. Robert, J. Quant. Spectrosc. Radiat. Transfer **37**, 531 (1987); A. Bauer, M. Godon, M. Kheddar, and J. M. Hartmann, *ibid.* **41**, 49 (1989).
[17] G. Chalisinski, M. M. Szczesniak, and S. Scheiner, J. Chem. Phys. **94**, 2807 (1991).
[18] M. Bulski, P. E. S. Wormer, and A. Van der Avoird, J. Chem. Phys. **94**, 8096 (1991).
[19] G. A. Blake, K. B. Laughlin, R. C. Cohen, K. L. Busarow, D-H. Gwo, C. A. Schmuttenmaer, D. W. Steyert, and R. J. Saykally, Rev. Sci. Instrum. **62**, 1693 (1991).
[20] G. A. Blake, K. B. Laughlin, R. C. Cohen, K. L. Busarow, D-H. Gwo, C. A. Schmuttenmaer, D. W. Steyert, and R. J. Saykally, Rev. Sci. Instrum. **62**, 1701 (1991).
[21] D. Kaur, A. M. de Souza, J. Wanna, S. A. Hammad, L. Mercorelli, and D. S. Perry, Appl. Opt. **29**, 119 (1990).
[22] K. L. Busarow, U. C. Berkeley, Ph.D. thesis, 1990.
[23] R. C. Cohen and R. J. Saykally (unpublished).
[24] J. M. Hutson, Adv. Mol. Vibrations Collision Dynamics **1**, 1 (1991).
[25] C. M. Lovejoy and D. J. Nesbitt, J. Chem. Phys. **91**, 2790 (1989).
[26] D. J. Nesbitt, M. S. Child, and D. C. Clary, J. Chem. Phys. **90**, 4855 (1989).
[27] C. A. Schmuttenmaer, R. C. Cohen, J. Loeser, and R. J. Saykally, J. Chem. Phys. **95**, 9 (1991).
[28] C. A. Schmuttenmaer, J. Loeser, and R. J. Saykally (unpublished).
[29] J. W. I. van Bladel, A. Van der Avoird, and P. E. S. Wormer, J. Phys. Chem. **95**, 5414 (1991).
[30] M. Bulski, P. E. S. Wormer, and A. Van der Avoird, J. Chem. Phys. **94**, 491 (1991).